Angle-domain elastic reverse-time migration

Jia Yan and Paul Sava
Center for Wave Phenomena Colorado School of Mines

ABSTRACT
Multi-component data are not usually processed with specifically designed procedures, but with procedures analogous to the ones used for single-component data. Commonly, the vertical and horizontal components of the data are taken as proxies for P and S wave modes which are imaged independently with the acoustic wave equation. This procedure works only if the vertical and horizontal component accurately represent P and S wave modes, which is not true in general. Therefore, multi-component images constructed with this procedure exhibit artifacts caused by the incorrect wave mode separation at the surface.
An alternative procedure for elastic imaging uses the vector fields for wavefield reconstruction and imaging. The wavefields are reconstructed using the multi-component data as boundary conditions for a numerical solution to the elastic wave equation. The key component for wavefield migration is the imaging condition that evaluates the match between wavefields reconstructed from sources and receivers. For vector wavefields, a simple component-by-component cross-correlation between two wavefields leads to artifacts caused by cross-talk between the unseparated wave modes. An alternative method is to separate elastic wavefields after reconstruction in the subsurface and implement the imaging condition as cross-correlation of pure wave modes instead of the Cartesian components of the displacement wavefield. This approach leads to images that are easier to interpret, since they describe reflectivity of specified wave modes at interfaces of physical properties.
As for imaging with acoustic wavefields, the elastic imaging condition can be formulated conventionally (cross-correlation with zero lag in space and time), as well as extended to non-zero space and time lags. The elastic images produced by an extended imaging condition can be used for angle decomposition of primary (PP or SS) and converted (PS or SP) reflectivity. Angle gathers constructed with this procedure have applications for migration velocity analysis and amplitude versus angle analysis.

Key words: imaging, elastic, reverse time

1 INTRODUCTION

Seismic processing is usually based on acoustic wave equations, which assume that the Earth represents a liquid that propagates only compressional waves. Although useful in practice, this assumption is not theoretically valid. Earth materials allow for both primary and shear wave propagation in the subsurface. Shear waves, either generated at the source or converted from compressional waves at various interfaces in the subsurface, are recorded by multi-component receivers. Shear waves are usually stronger at large incidence and reflection angles, often corresponding to large offsets. However, for complex geological structures near the surface, shear waves can be quite significant even at small offsets. Conventional single-component imaging ignores shear wave modes, which often leads to incorrect characterization of wave-propagation, incomplete illumination of the subsurface and poor amplitude characterization, etc.

Even when multi-component data are used for imaging, they are usually not processed with specifically designed procedures. Instead, those data are processed with ad-hoc procedures borrowed from acoustic wave equation imaging algorithms. A typical assumption is that the recorded vertical and horizontal components are good approximations for the P and S wave modes, respectively, which can be imaged independently. This assumption is not always correct, leading to errors

and noise in the images, since P and S wave modes are normally mixed on all recorded components. Also, since P and S modes are mixed on all components, true-amplitude imaging is questionable no matter how accurate the wavefield reconstruction and imaging condition are.

Multi-component imaging has long been an active research area for exploration geophysicists. Techniques proposed in the literature perform imaging in the time domain, e.g. by Kirchhoff migration (Kuo & Dai, 1984; Hokstad, 2000) and reverse time migration (Chang & McMechan, 1986, 1994) adapted for multi-component data. The reason for working in the time domain, as opposed to the depth domain, is that the coupling of displacements in different directions in elastic wave equations makes it difficult to derive a dispersion relation that can be used to extrapolate wavefields in depth.

Early attempts at multi-component imaging use the Kirchhoff framework. Kuo & Dai (1984) perform shot-profile elastic Kirchhoff migration and Hokstad (2000) performs survey-sinking elastic Kirchhoff migration. Although these techniques represent different migration procedures, they compute travel-times for both PP and PS reflections, and sum data along these travel time trajectories. This approach is equivalent to distinguishing between PP reflection and PS reflections, and applying acoustic Kirchhoff migration for each mode separately. When geology is complex, the elastic Kirchhoff migration technique suffers from drawbacks similar to those of acoustic Kirchhoff migration because ray theory breaks down (Gray *et al.*, 2001).

There are two main difficulties with independently imaging P and S wave modes separated on the surface. The first is that conventional elastic migration techniques either consider vertical and horizontal components of recorded data as P and S modes, which is not always accurate, or separate these wave modes on the recording surface using approximations, e.g. polarization (Pestana *et al.*, 1989) or elastic potentials (Etgen, 1988; Zhe & Greenhalgh, 1997). Other elastic reverse time migration techniques do not separate wave modes on the surface and reconstruct vector fields, but use imaging conditions based on ray tracing (Chang & McMechan, 1986, 1994) that are not always robust in complex geology. The second difficulty is that images produced independently from P and S modes are hard to interpret together, since often they do not line-up consistently, thus requiring image post processing, e.g. by manual or automatic registration of the images (Fomel & Backus, 2003; Nickel & Sonneland, 2004).

We advocate an alternative procedure for imaging elastic wavefield data. Instead of separating wavefields into scalar wave modes on the acquisition surface followed by scalar imaging of each mode independently, we use the entire vector wavefields for wavefield reconstruction and imaging. The vector wavefields are reconstructed using the multi-component vector data as boundary conditions for a numerical solution to the elastic wave equation. The key component of such a migration procedure is the imaging condition which evaluates the match between wavefields reconstructed from the source and receiver. For vector wavefields, a simple component-by-component cross-correlation between the two wavefields leads to artifacts caused by cross-talk between the unseparated wave modes, i.e. all P and S modes from the source wavefield correlate with all P and S modes from the receiver wavefield. This problem can be alleviated by using separated elastic wavefields, with the imaging condition implemented as cross-correlation of wave modes instead of cross-correlation of the Cartesian components of the wavefield. This approach leads to images that are cleaner and easier to interpret since they represent reflections of single wave modes at interfaces of physical properties.

As for imaging with acoustic wavefields, the elastic imaging condition can be formulated conventionally (cross-correlation with zero lag in space and time), as well as extended to non-zero space lags. The elastic images produced by extended imaging condition can be used for angle decomposition of PP and PS reflectivity. Angle gathers have many applications, including migration velocity analysis (MVA) and amplitude versus angle (AVA) analysis.

The advantage of imaging with multi-component seismic data is that the physics of wave propagation is better represented, and resulting seismic images more accurately characterize the subsurface. Multi-component images have many applications. For example they can be used to provide reflection images where the P-wave reflectivity is small, image through gas clouds where the P-wave signal is attenuated, detect fractures through shear-wave splitting, validate bright spot reflections and provide parameter estimation for this media, and Poisson's ratio estimates (Simmons & Backus, 2003). Assuming no attenuation in the subsurface, converted wave images also have higher resolution than pure-mode images in shallow part of sections, because S waves have shorter wavelengths than P waves. Modeling and migrating multi-component data with elastic migration algorithms, enables us to make full use of information provided by elastic data, and correctly positions geologic structures.

We begin by summarizing wavefield imaging methodology, focusing on reverse-time migration for wavefield multi-component migration. Then, we describe different options for wavefield multi-component imaging conditions, e.g. based on vector displacements and vector potentials. Finally, we describe the application of extended imaging condition to multi-component data and corresponding angle decomposition. We illustrate the wavefield imaging techniques using data simulated on the Marmousi II model (Martin *et al.*, 2002).

2 WAVEFIELD IMAGING

Seismic imaging is based on numerical solutions to wave equations, which can be classified into ray-based (integral) solutions and wavefield-based (differential) solutions. Kirchhoff migration is a typical ray-based imaging procedure which is computationally efficient but often fails in areas of complex geology, such as sub-salt, because the wavefield is severely distorted by lateral velocity variations leading to complex multipathing. Wavefield imaging works better for complex geology, but is more expensive than Kirchhoff migration. Depending on computational time constraints and available re-

sources, different levels of approximation are applied to accelerate imaging, i.e. one-way vs. two-way, acoustic vs. elastic, isotropic vs. anisotropic, etc.

Despite the complexity of various types of wavefield migration algorithms, any wavefield imaging can be separated into two parts: wavefield reconstruction followed by the application of an imaging condition. For prestack depth migration, source and receiver wavefields have to be reconstructed at all locations in the subsurface. The wavefield reconstruction can be done in both depth and time domain, and with different modeling approaches, such as finite-difference (Dablain, 1986; Alford *et al.*, 1990), finite-element (Bolt & Smith, 1976), spectral method (Seriani & Priolo, 1991; Seriani *et al.*, 1992; Dai & Cheadle, 1996), etc. After reconstructing wavefields with the recorded data as boundary conditions into the subsurface, an imaging condition must be applied at all locations in the subsurface in order to obtain a seismic image. The simplest types of imaging condition are based on cross-correlation or deconvolution of the reconstructed wavefields (Claerbout, 1971). These imaging conditions can be implemented in the time or frequency domains, depending on the domain in which wavefields have been reconstructed. Here, we concentrate on reverse-time migration with wavefield reconstruction and imaging condition implemented in the time domain.

2. 1 Reverse-time migration

Reverse-time migration reconstructs the source wavefield forward in time and the receiver wavefield backward in time. It then applies an imaging condition to extract reflectivity information out of the reconstructed wavefields. The advantages of reverse-time migration over other depth migration techniques are that the extrapolation in time does not involve evanescent energy, and no dip limitations exist for the imaged structures. Although conceptually simple, reverse-time migration has not been used extensively in practice due to its high computational cost. However, the algorithm is becoming more and more attractive to the industry because of its robustness in imaging complex geology, e.g. sub-salt Jones *et al.* (2007); Boechat *et al.* (2007).

Whitmore (1983) and Baysal *et al.* (1983) first used reverse-time migration for poststack or zero-offset data. The procedure of poststack reverse-time migration is the following: first, reverse the recorded data in time; second, use these reversed data as sources along the recording surface to propagate the wavefields in the subsurface; third, extract the image at zero time, e.g. apply an imaging condition. The principle of poststack reverse-time migration is that the subsurface reflectors work as exploding reflectors and that the wave equation used to propagate data can be applied either forward or backward in time by simply reversing the time axis (Levin, 1984).

Chang & McMechan (1986) apply reverse-time migration to prestack data. Prestack reverse-time migration reconstructs source and receiver wavefields. The source wavefield is reconstructed forward in time, and the receiver wavefield is reconstructed backward in time. Chang & McMechan (1986, 1994) use a so called excitation-time imaging condition, where images are formed by extracting the receiver wavefield at the time taken by a wave to travel from the source to the image point. This imaging condition is a special case of the cross-correlation imaging condition of Claerbout (1971).

2. 2 Elastic imaging vs. acoustic imaging

Multi-component elastic data are often recorded in land or marine (ocean-bottom) seismic experiments. However, as mentioned earlier, elastic vector wavefields are not usually processed by specifically designed imaging procedures, but rather by extensions of techniques used for scalar wavefields. Thus, seismic data processing does not take full advantage of the information contained by elastic wavefields. In other words, it does not fully illuminate complex geology or correctly preserve imaging amplitudes and estimate model parameters, etc.

Elastic wave propagation in a homogeneous and arbitrarily anisotropic medium is characterized by the wave equation

$$\rho \frac{\partial^2 u_i}{\partial t^2} - c_{ijkl} \frac{\partial^2 u_k}{\partial x_j \partial x_l} = f_i \ , \tag{1}$$

where u_i is the component i of the displacement vector $\mathbf{u}$, ρ is the density, c_{ijkl} is the stiffness tensor and f_i are the Cartesian components of the vector source $\mathbf{f}\,(t)$. This wave equation assumes a slowly varying stiffness tensor over the imaging space. The coupling of displacements for different directions in the wave equation 1 makes it difficult to derive a dispersion relation that can be used to extrapolate wavefields in depth. This makes it natural to process elastic wavefields in time. There are two main options for elastic imaging in the time domain: Kirchhoff migration and reverse-time migration.

Acoustic Kirchhoff migration is based on diffraction summation, which accumulates the data along diffraction curves in the data space and maps them onto the image space. For multi-component elastic data, Kuo & Dai (1984) discuss Kirchhoff migration for shot-record data. Here, identified PP and PS reflections can be migrated by computing source and receiver traveltimes using P wave velocity for the source rays, and P and S wave velocities for the receiver rays. Hokstad (2000) performs multi-component anisotropic Kirchhoff migration for multi-shot, multi-receiver experiments, where pure-mode and converted mode images are obtained by downward continuation of visco-elastic vector wavefields and application of survey-sinking imaging condition to the reconstructed vector wavefields. The wavefield separation is effectively done by the Kirchhoff integral which handles both P- and S-waves, although this technique fails in areas of complex geology where ray theory breaks down.

Elastic reverse-time migration has the same two components as acoustic reverse-time migration: reconstruction of source and receiver wavefield and application of an imaging condition. The source and receiver wavefields are reconstructed by forward and backward propagation in time with various modeling approaches. For acoustic reverse-time migration, wavefield reconstruction is done with the acoustic wave-equation using the recorded scalar data as boundary con-

dition. In contrast, for elastic reverse-time migration, wavefield reconstruction is done with the elastic wave-equation using the recorded vector data as boundary condition.

Since pure-mode and converted-mode reflections are mixed on all components of recorded data, images produced with reconstructed elastic wavefields are characterized by cross-talk due to the interference of various wave modes. In order to obtain images with clear physical meanings, most imaging conditions separate wave modes, because they are mixed in all components of the data. There are two potential approaches to separate wavefields and image elastic seismic wavefields. The first option is to separate P and S modes on the acquisition surface from the recorded elastic wavefields. This procedure involves either approximations for the propagation path and polarization direction of the recorded data, or reconstruction of the seismic wavefields in the vicinity of the acquisition surface by a numerical solution of the elastic wave equation, followed by wavefield separation of scalar and vector potentials using Helmholtz decomposition (Etgen, 1988; Zhe & Greenhalgh, 1997). An alternative data decomposition using P and S potentials is to reconstruct wavefields in the subsurface using the elastic wave equation, then decompose the wavefields in P and S wave modes. This is followed by forward extrapolating the separated wavefields back to the surface using the acoustic wave equation with the appropriate propagation velocity for the various wave modes (Sun *et al.*, 2006) by conventional procedures used for scalar wavefields.

The second option is to extrapolate wavefields in the subsurface using a numeric solution to the elastic wave equation and then apply an imaging condition that extracts reflectivity information from the source and receiver wavefields. In case extrapolation is implemented by finite-difference methods (Chang & McMechan, 1986, 1994), this procedure is known as elastic reverse-time migration, and is conceptually similar to acoustic reverse-time migration (Baysal *et al.*, 1983), which is more frequently used in seismic imaging.

Many imaging conditions can be used for reverse-time migration. The elastic imaging condition is more complex than acoustic imaging condition because both source and receiver wavefields are vector fields. Different elastic imaging conditions have been proposed for extracting reflectivity information from reconstructed elastic wavefields. For example, Hokstad *et al.* (1998) use elastic reverse-time migration with Lamé potential methods. Chang & McMechan (1986) use the excitation-time imaging condition which extracts reflectivity information from extrapolated wavefields at traveltimes from the source to image positions computed by ray tracing, etc. Ultimately, these imaging conditions represent special cases of a more general type of imaging condition that involves time cross-correlation or deconvolution of source and receiver wavefields at every location in the subsurface.

3 CONVENTIONAL ELASTIC IMAGING CONDITIONS

For vector elastic wavefields, the cross-correlation imaging condition needs to be implemented on all components of the displacement field. The problem with this type of imaging condition is that the source and receiver wavefields contain a mix of P and S wave modes which cross-correlate independently, thus hampering interpretation of migrated images. An alternative to this type of imaging is to perform wavefield separation of scalar and vector potentials after wavefield reconstruction in the imaging volume, but prior to the imaging condition and then cross-correlate pure modes from the source and receiver wavefields, as suggested by Dellinger & Etgen (1990) and illustrated by Cunha Filho (1992).

3. 1 Imaging with scalar wavefields

As mentioned earlier, assuming single scattering in the Earth (Born approximation), a conventional imaging procedure consists of two components: wavefield extrapolation and imaging. Wavefield extrapolation is used to reconstruct in the imaging volume the seismic wavefield using the recorded data on the acquisition surface as boundary condition, and imaging is used to extract reflectivity information from the extrapolated source and receiver wavefields.

Assuming scalar recorded data, wavefield extrapolation using a scalar wave equation reconstructs scalar source and receiver wavefields, $u_s\left(\mathbf{x},t\right)$ and $u_r\left(\mathbf{x},t\right)$, at every location in the subsurface. Using the extrapolated scalar wavefields, a conventional imaging condition (Claerbout, 1985) can be implemented as cross-correlation at zero-lag time:

$$I\left(\mathbf{x}\right)=\int u_s\left(\mathbf{x},t\right)u_r\left(\mathbf{x},t\right)dt\ . \tag{2}$$

Here, $I\left(\mathbf{x}\right)$ denotes a scalar image obtained from scalar wavefields $u_s\left(\mathbf{x},t\right)$ and $u_r\left(\mathbf{x},t\right)$, $\mathbf{x}=\{x,y,z\}$ represent Cartesian space coordinates, and t represents time.

3. 2 Imaging with vector displacements

Assuming vector recorded data, wavefield extrapolation using a vector wave equation reconstructs source and receiver wavefields $\mathbf{u}_s\left(\mathbf{x},t\right)$ and $\mathbf{u}_r\left(\mathbf{x},t\right)$ at every location in the subsurface. Here, $\mathbf{u}_s$ and $\mathbf{u}_r$ represent displacement fields reconstructed from data recorded by multi-component geophones at the surface boundary. Using the vector extrapolated wavefields $\mathbf{u}_s=\{u_{sx},u_{sy},u_{sz}\}$ and $\mathbf{u}_r=\{u_{rx},u_{ry},u_{rz}\}$, an imaging condition can be formulated as a straightforward extension of 2 by cross-correlating all combinations of components of the source and receiver wavefields. Such an imaging condition for vector displacements can be formulated mathematically as

$$I_{ij}\left(\mathbf{x}\right)=\int u_{si}\left(\mathbf{x},t\right)u_{rj}\left(\mathbf{x},t\right)dt\ , \tag{3}$$

where the quantities u_i and u_j stand for the Cartesian components x,y,z of the vector source and receiver wavefields, $\mathbf{u}\left(\mathbf{x},t\right)$. For example, $I_{zz}\left(\mathbf{x}\right)$ represents the image component produced by cross-correlation of the z components of the source and receiver wavefields, $I_{zx}\left(\mathbf{x}\right)$ represents the image component produced by cross-correlation of the z component of the source wavefield with the x component of the receiver

wavefield, etc. In general, an image produced with this procedure has 9 components at every location in space.

The main drawback of applying this type of imaging condition is that the wavefield used for imaging contain a combination of P and S wave modes. Those wavefield vectors interfere with one-another in the imaging condition, since the P and S components are not separated in the extrapolated wavefields. The cross-talk between various components of the wavefield creates artifacts and makes it difficult to interpret the images in terms of pure wave modes, e.g. PP or PS reflections. This situation is similar to the case of imaging with acoustic data contaminated by multiples or other types of coherent noise which are mapped in the subsurface using incorrect velocity.

3. 3 Imaging with scalar and vector potentials

An alternative to the elastic imaging condition 3 is to separate the extrapolated wavefield in P and S potentials after extrapolation and image using cross-correlations of vector and scalar potentials (Dellinger & Etgen, 1990). Separation of scalar and vector potentials can be achieved by Helmholtz decomposition, which is applicable to any vector field $\mathbf{u}(\mathbf{x},t)$:

$$\mathbf{u} = \nabla\Phi + \nabla\times\mathbf{\Psi}\ , \tag{4}$$

where $\Phi(\mathbf{x},t)$ represents the scalar potential of the wavefield $\mathbf{u}(\mathbf{x},t)$ and $\mathbf{\Psi}(\mathbf{x},t)$ represents the vector potential of the wavefield $\mathbf{u}(\mathbf{x},t)$. For isotropic elastic wavefields, equation 4 is not used directly in practice, but the scalar and vector components are obtained indirectly by the application of the divergence ($\nabla\cdot$) and curl ($\nabla\times$) operators to the extrapolated elastic wavefield $\mathbf{u}(\mathbf{x},t)$:

$$P = \nabla\cdot\mathbf{u} = \nabla^2\Phi\ , \tag{5}$$

$$\mathbf{S} = \nabla\times\mathbf{u} = -\nabla^2\mathbf{\Psi}\ . \tag{6}$$

For isotropic elastic fields far from the source, quantities P and $\mathbf{S}$ describe compressional and shear components of the wavefield, respectively (Aki & Richards, 2002).

Using the separated scalar and vector components, we can formulate an imaging condition that combines various incident and reflected wave modes. The imaging condition for vector potentials can be formulated mathematically as

$$I_{ij}(\mathbf{x}) = \int \alpha_{si}(\mathbf{x},t)\,\alpha_{rj}(\mathbf{x},t)\,dt\ , \tag{7}$$

where the quantities α_i and α_j stand for the various wave modes $\alpha = \{P, S_1, S_2\}$ of the vector source and receiver wavefields, $\mathbf{u}(\mathbf{x},t)$. For example, $I_{PP}(\mathbf{x})$ represents the image component produced by cross-correlation of the P wave mode of the source and receiver wavefields, $I_{PS_1}(\mathbf{x})$ represents the image component produced by cross-correlation of the P wave mode of the source wavefield with the S_1 wave-mode of the receiver wavefield, etc. In general, an image produced with this procedure also has 9 components at every location in space, similarly to the image produced by the cross-correlation of the various Cartesian components of the vector displacements. However, in this case, the images correspond to various combinations of incident P or S and reflected P or S waves, thus having clear physical meaning and being easier to interpret for physical properties.

4 EXTENDED ELASTIC IMAGING CONDITIONS

The conventional imaging condition 2 discussed in the preceding section uses the zero lag of the cross-correlation between the source and receiver wavefields. This imaging condition represents a special case of a more general form of imaging condition, sometimes referred-to as an extended imaging condition (Sava & Fomel, 2006b)

$$I_{ij}(\mathbf{x},\boldsymbol{\lambda},\tau) = \int u_s(\mathbf{x}-\boldsymbol{\lambda},t-\tau)\,u_r(\mathbf{x}+\boldsymbol{\lambda},t+\tau)\,dt\ , \tag{8}$$

where $\boldsymbol{\lambda} = \{\lambda_x,\lambda_y,\lambda_z\}$ and τ stand for cross-correlation lags in space and time, respectively. The imaging condition 2 is equivalent with the extended imaging condition 8 for $\boldsymbol{\lambda} = \mathbf{0}$ and $\tau = 0$.

The extended imaging condition has two main uses. First, the extended imaging condition characterizes wavefield reconstruction errors, since for incorrectly reconstructed wavefields, the cross-correlation energy does not focus completely at zero lags in space and time. Sources of wavefield reconstruction error include inaccurate numeric solutions to the wave-equation, inaccurate (velocity) models used for wavefield reconstruction, inadequate wavefield sampling on the acquisition surface, uneven illumination of the subsurface, etc. Typically, all these causes of inaccurate wavefield reconstruction occur simultaneously and it is difficult to separate them after imaging. Second, assuming accurate wavefield reconstruction, the extended imaging condition can be used for angle decomposition. This leads to representations of reflectivity function of angles of incidence and reflection at all points in the imaged volume (Sava & Fomel, 2003). Here, we assume that wavefield reconstruction is accurate and concentrate on further extensions of the imaging condition, such as angle decomposition.

4. 1 Imaging with vector displacements

For the case of imaging with vector wavefields, the extended imaging condition 8 can be applied directly to the various components of the reconstructed source and receiver wavefields, similarly to the conventional imaging procedure described in the preceding section. Therefore, an extended image constructed from vector displacement wavefields is

$$I_{ij}(\mathbf{x},\boldsymbol{\lambda},\tau) = \int u_{si}(\mathbf{x}-\boldsymbol{\lambda},t-\tau)\,u_{rj}(\mathbf{x}+\boldsymbol{\lambda},t+\tau)\,dt\ , \tag{9}$$

where the quantities u_{si} and u_{rj} stand for the Cartesian components x,y,z of the vector source and receiver wavefields, and $\boldsymbol{\lambda}$ and τ stand for cross-correlation lags in space and time, respectively. This imaging condition suffers from the same drawbacks described for the similar conventional imaging condition applied to the Cartesian components of the reconstructed wavefields, i.e. cross-talk between the unseparated wave modes, etc.

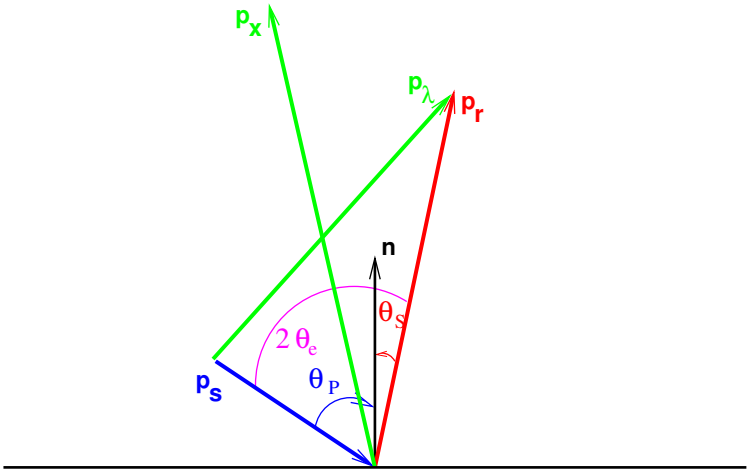


Figure 1. Local wave vectors of the converted wave at a common image point location in 3D. The plot shows the conversion in the reflection plane in 2D. $\mathbf{p_s}$, $\mathbf{p_r}$, $\mathbf{p_x}$ and $\mathbf{p_\lambda}$ are ray parameter vectors for the source ray, receiver ray, and combinations of the two. The length of the incidence and reflection wave vectors are inversely proportional to the incidence and reflection wave velocity, respectively. Vector $\mathbf{n}$ is the normal of the reflector. By definition, $\mathbf{p_x} = \mathbf{p_r} + \mathbf{p_s}$ and $\mathbf{p_\lambda} = \mathbf{p_r} - \mathbf{p_s}$.

4. 2 Imaging with scalar and vector potentials

An extended imaging condition can also be designed for elastic wavefields decomposed in scalar and vector potentials, similarly to the conventional imaging procedure described in the preceding section. Therefore, an extended image constructed from scalar and vector potentials is

$$I_{ij}\left(\mathbf{x},\boldsymbol{\lambda},\tau\right) = \int \alpha_{si}\left(\mathbf{x}-\boldsymbol{\lambda},t-\tau\right)\alpha_{rj}\left(\mathbf{x}+\boldsymbol{\lambda},t+\tau\right)dt\ , \tag{10}$$

where the quantities α_{si} and α_{rj} stand for the various wave modes $\alpha = \{P, S_1, S_2\}$ of the source and receiver wavefields, and $\boldsymbol{\lambda}$ and τ stand for cross-correlation lags in space and time, respectively.

5 ANGLE DECOMPOSITION

As indicated earlier, the main uses of images constructed using extended imaging conditions are migration velocity analysis (MVA) and amplitude versus angle analysis (AVA). Such analysis, however, require that the images be decomposed in components corresponding to various angles of incidence, procedure which is often referred to as angle decomposition. Angle decomposition takes different forms corresponding to the type of wavefields involved in imaging. Thus, we can distinguish angle decomposition for scalar (acoustic) wavefields and angle decomposition for vector (elastic) wavefields.

5. 1 Scalar wavefields

For the case of imaging with the acoustic wave equation, the reflection angle corresponding to incidence and reflection of P wave modes can be constructed after imaging using mapping based on the relation

$$\tan\theta_a = \frac{|\mathbf{k_\lambda}|}{|\mathbf{k_x}|}\ , \tag{11}$$

where θ_a is the incidence angle and $\mathbf{k_x} = \mathbf{k_r} + \mathbf{k_s}$ and $\mathbf{k_\lambda} = \mathbf{k_r} - \mathbf{k_s}$ are defined using the source and receiver wavenumbers, $\mathbf{k_s}$ and $\mathbf{k_r}$. The information required for decomposition of the reconstructed wavefields as a function of wavenumbers $\mathbf{k_x}$ and $\mathbf{k_\lambda}$ is readily available in the images $I\left(\mathbf{x},\boldsymbol{\lambda},\tau\right)$ constructed by extended imaging conditions 9 or 10. Following angle decomposition, the image $I\left(\mathbf{x},\theta,\phi\right)$ represents a mapping of the image $I\left(\mathbf{x},\boldsymbol{\lambda},\tau\right)$ from offsets to angles. In other words, all information for characterizing angle-dependent reflectivity is already available in the image obtained by the extended imaging conditions.

5. 2 Vector wavefields

A similar approach can be used for decomposition of the reflectivity as a function of incidence and reflection angles for elastic wavefields imaged with extended imaging conditions 9 or 10. The angle θ_e characterizing the average angle between incidence and reflected rays can be computed using the expression:

$$\tan^2\theta_e = \frac{\left(1+\gamma\right)|\mathbf{k_\lambda}|^2 - \left(1-\gamma\right)|\mathbf{k_x}|^2}{\left(1+\gamma\right)|\mathbf{k_x}|^2 - \left(1-\gamma\right)|\mathbf{k_\lambda}|^2}\ , \tag{12}$$

where γ is the velocity ratio of the incident and reflected waves, e.g. v_p/v_s ratio for incident P mode and reflected S mode. Figure 1 shows the schematic and the notations used in the above formula. The angle decomposition equation 12 designed for PS reflections reduces to equation 11 for PP reflections when $\gamma = 1$.

Angle decomposition using equation 12 requires computation of extended imaging condition with 3-D space lags $(\lambda_x, \lambda_y, \lambda_z)$, which is computationally costly. Faster computation can be done if we avoid computing the vertical lag λ_z, in which case the angle decomposition can be done using the expression (Sava & Fomel, 2006a):

$$\tan\theta_e = \frac{\left(1+\gamma\right)\left(a_{\lambda_x}+b_x\right)}{2\gamma\ k_z + \sqrt{4\gamma^2k_z^2 + \left(\gamma^2-1\right)\left(a_{\lambda_x}+b_x\right)\left(a_x+b_{\lambda_x}\right)}}\ , \tag{13}$$

where $a_{\lambda_x} = \left(1+\gamma\right)k_{\lambda_x}$, $a_x = \left(1+\gamma\right)k_x$, $b_{\lambda_x} = \left(1-\gamma\right)k_{\lambda_x}$, and $b_x = \left(1-\gamma\right)k_x$. Figure 2 shows a model of five reflectors and the extracted angle gathers for these re-

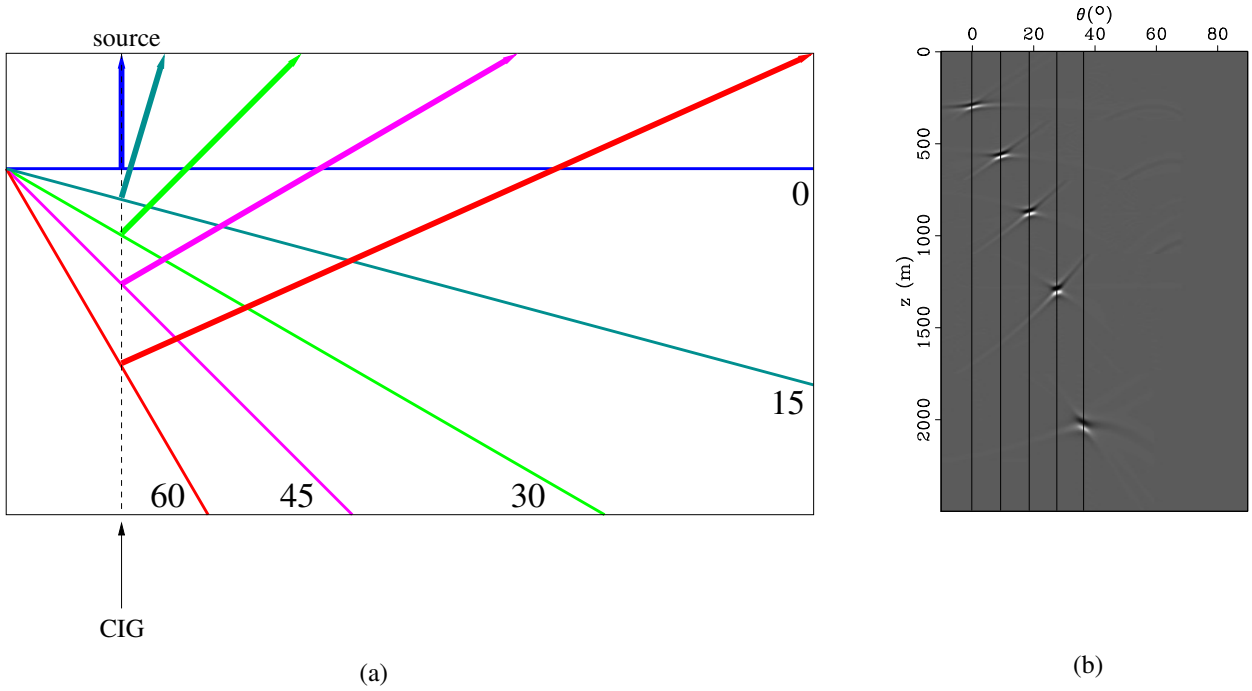


Figure 2. (a) Model showing one shot over multiple reflectors dipping at 0°, 15°, 30°, 45° and 60°. The vertical dashed line shows a CIG location. Incidence ray is vertically down and P to S conversions are marked by arrowed liens pointing away from reflectors. (b) Converted wave angle gather obtained from algorithm described by Sava & Fomel (2006a). Notice that converted wave angles are always smaller than incidence angle (in this case, the dip of the reflector) except for normal incidence.

flectors at the location of the source. For PP reflections, the reflections would occur in the angle gather at an angle equal with the reflector slope. However, for PS reflections, illustrated in Figure 2, the reflection angle is smaller than the reflector slope, as expected.

6 EXAMPLES

We test the different imaging conditions discussed in the preceding sections with data simulated on a modified subset of the Marmousi II model (Martin *et al.*, 2002). The section is chosen to be at the left side of the entire model which is relatively simple and therefore easier to examine the quality of the images.

6. 1 Imaging with vector displacements

Consider the images obtained for the model depicted in Figures 3(a) & 3(b). Figure 3(a) depicts the P-wave velocity (smooth function between $1.6 - 3.2$ km/s), and Figure 3(b) shows the density (variable between $1 - 2$ g/cm^3). The S-wave velocity is a scaled version of the P-wave velocity with $v_p/v_s = 2$. Data are modeled and migrated in the smooth velocity background to avoid back-scattering and the migration density is constant throughout the model. Elastic data, Figures 4(a) & 4(b), are simulated using a space-time staggered-grid finite-difference solution to the isotropic elastic wave equation (Virieux, 1984, 1986; Mora, 1987, 1988). We simulate data for a source located at position $x = 6.75$ km and $z = 0.5$ km. Since we are using an explosive source and the background velocity is smooth, the simulated wavefield is represented mainly by P-wave incident energy and the receiver wavefield is represented by a combination of P- and S-wave reflected energy. The data contain a mix of P and S modes, as can be seen by comparing the vertical and horizontal displacement components, shown in Figures 4(a) & 4(b), with the separated P and S wave modes, shown in Figures 4(c) & 4(d).

Imaging the data shown in Figures 4(a) & 4(b) using the imaging condition 3, we obtain the images depicted in Figures 5(a) & 5(d). Since the input data do not represent separated wave modes, the images produced with the imaging condition based on vector displacements do not separate PP and PS reflectivity. Thus, the images are hard to interpret, since it is not clear what incident and reflected wave mode the reflections correspond to. In reality, reflections corresponding to all wave modes are present in all panels.

6. 2 Imaging with scalar and vector potentials

Consider the images (Figures 6) obtained for imaging condition equations 7 applied to the data (Figures 4(a) and 4(b)) used for the preceding example. Given the explosive source used in our simulation, the source wavefield contains mostly

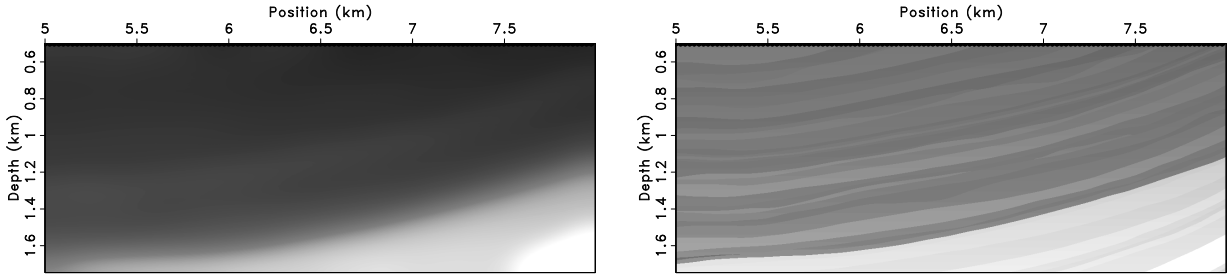


Figure 3. (a) V_P and V_s wave velocity models and (b) density model used for isotropic elastic wavefield modeling, where v_p ranges from 1.6 to 3.2 km/s from top to bottom and $v_p/v_s = 2$, and density ranges from 1 to 2 g/cm^3 .

P-wave energy, while the receiver wavefield contains P- and S-wave mode energy. Helmholtz decomposition after extrapolation but prior to imaging isolates P and S wavefield components. Therefore, migration produces images of reflectivity corresponding to PP and PS reflections, Figures 6(a) and 6(b), but not reflectivity corresponding to SP or SS reflections, Figures 6(c) and 6(d). The illumination regions are different between PP and PS images, due to different illumination angles of the two propagation modes for the given acquisition geometry. The PS image, Figure 6(b), also shows the usual polarity reversal for positive and negative angles of incidence measured relative to the reflector normal.

6. 3 Angle decomposition

The images shown in the preceding subsection correspond to the conventional imaging conditions 3 and 7. We can construct other images using the extended imaging conditions 9 and 10, which can be used for angle decomposition after imaging. Then, we can use equation 13 to compute angle gathers from horizontal space cross-correlation lags.

Figures 7(a) & 7(c) and Figures 7(b) & 7(d) show, respectively, the PP and PS horizontal lags and angle gathers for the common image gather (CIG) location in the middle of the reflectivity model, given a single source at $x = 6.75$ km. PP and PS horizontal lags are lines dipping at angles related to the incidence angle at the CIG location. PP angles are larger than PS angles at all reflectors, as illustrated on the simple synthetic example shown in Figure 2.

Figures 8(a) & 8(c) and Figures 8(b) & 8(d) show , respectively, the PP and PS horizontal lags and angle gathers for the same CIG location, given many sources from $x = 5.5$ to 7.5 km. The horizontal space cross-correlation lags are focused around $\boldsymbol{\lambda} = \mathbf{0}$, which justifies the use of conventional imaging condition extracting the cross-correlation of the source and receiver wavefields at zero lag in space and time. Thus, the zero lag of the images obtained by extended imaging condition represent the image at the particular CIG location. The PP and PS gathers for many sources are flat, since the migration was done with correct migration velocity. The PS angle gather, depicted in Figure 8(d), shows a polarity reversal at $\theta = 0$, which is consistent with the fact that PS images change polarity at normal incidence.

7 CONCLUSIONS

The elastic reverse time migration and related imaging conditions can be used for imaging and constructing angle domain common image gathers. Those techniques can be utilized in processing of land, ocean-bottom (OBC) and VSP multicomponent data.

The elastic reverse-time migration imaging condition can be formulated using decomposition of extrapolated wavefields in P and S wave modes. The formed images separate reflections corresponding to forward-propagating P or S modes and backward propagating P or S modes. In contrast, images formed by simple cross-correlation of displacement wavefield components mix contributions from P and S reflections and are harder to interpret. Artifacts caused by back-propagating the recorded data with displacement sources are present in both types of images, although they are easier to distinguish and attenuate on the images constructed with elastic components separated prior to imaging.

Extended imaging conditions can be applied to multicomponent images constructed using vector potentials. Angle decomposition allows for separation of reflectivity function of incidence and reflection angles. Angle-dependent reflectivity can be used for migration velocity analysis (MVA) and amplitude versus angle (AVA) analysis, which are extensions that fall outside the scope of this paper.

ACKNOWLEDGMENT

We acknowledge the support of the sponsors of the Consortium Project at the Center for Wave Phenomena at Colorado School of Mines.

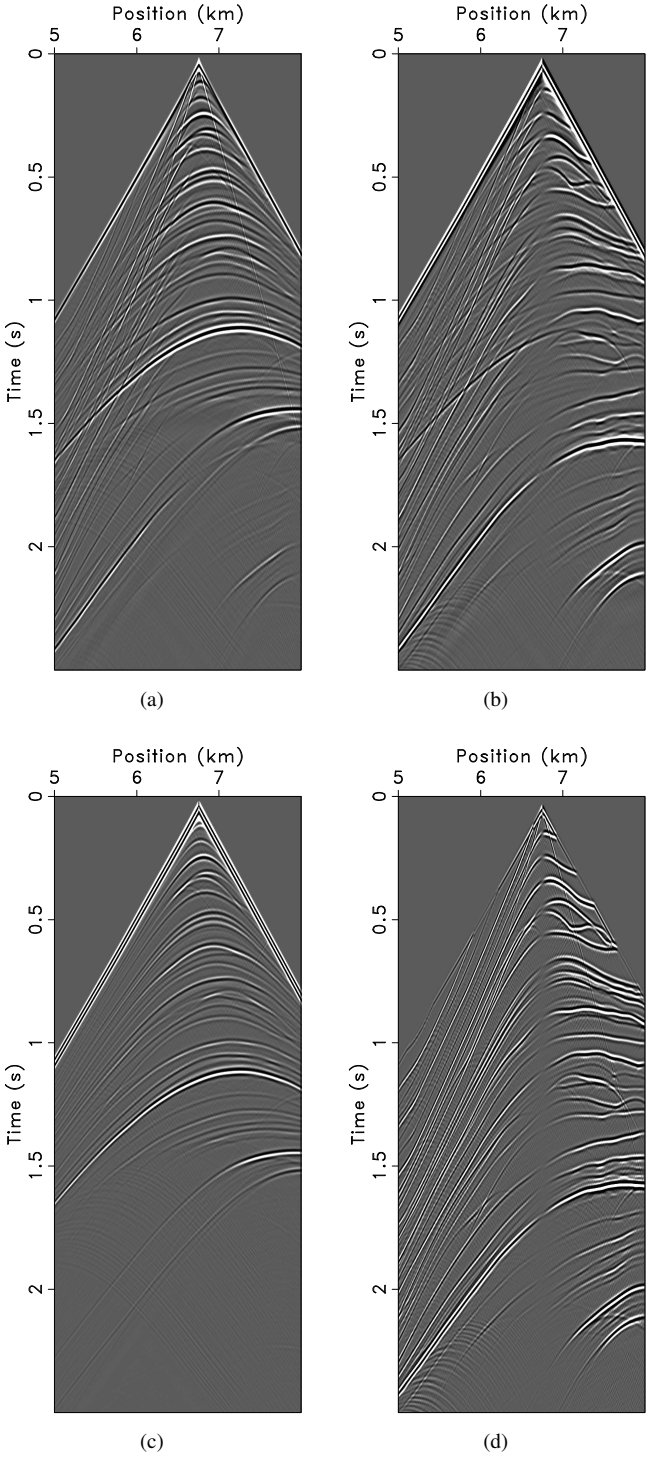


Figure 4. Elastic data simulated in model 3(a) and 3(b) with a source at $x = 6.75$ km and $z = 0.5$ km, and receivers at $z = 0.5$ km: (a) vertical component, (b) horizontal component, (c) scalar potential and (d) vector potential of the elastic wavefield. Both vertical and horizontal components, panels (a) and (b), contain a mix of P and S modes, as seen by comparison with panels (c) and (d).

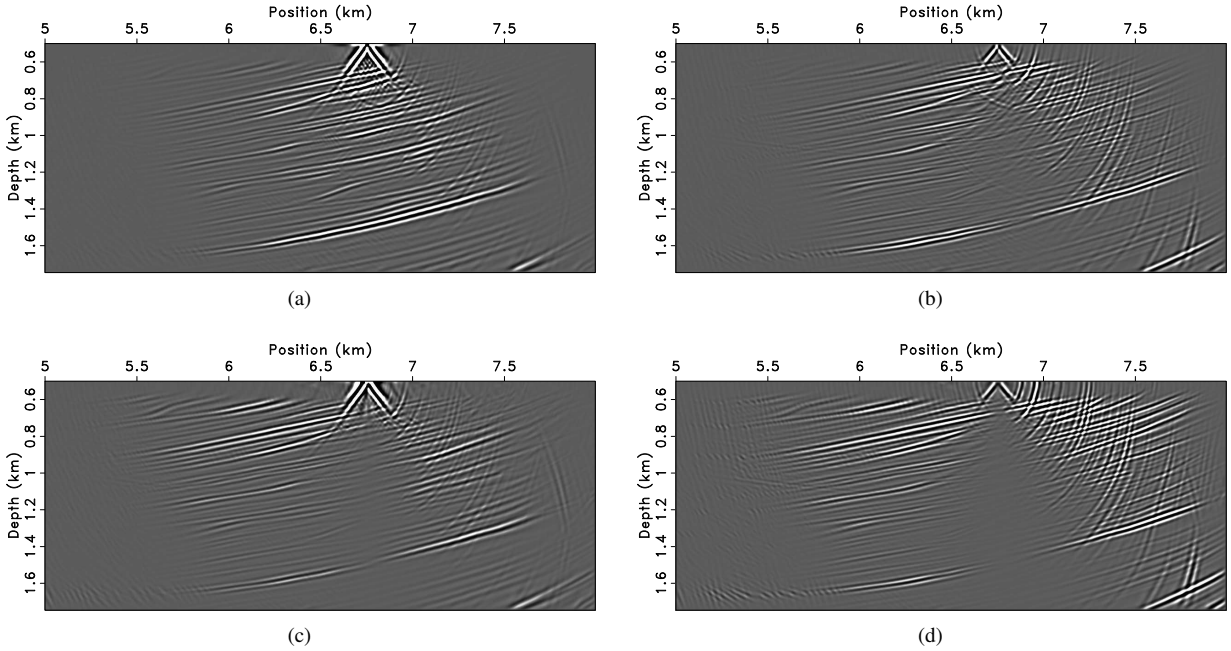


Figure 5. Images produced with the displacement components imaging condition, equation 3. (a), (b), (c) and (d) correspond to the cross-correlation of the vertical and horizontal components of the source wavefield with the vertical and horizontal components of the receiver wavefield, respectively. The image corresponds to one shot at position $x = 6.75$ km and $z = 0.5$ km. Receivers are located at all locations at $z = 0.5$ km.

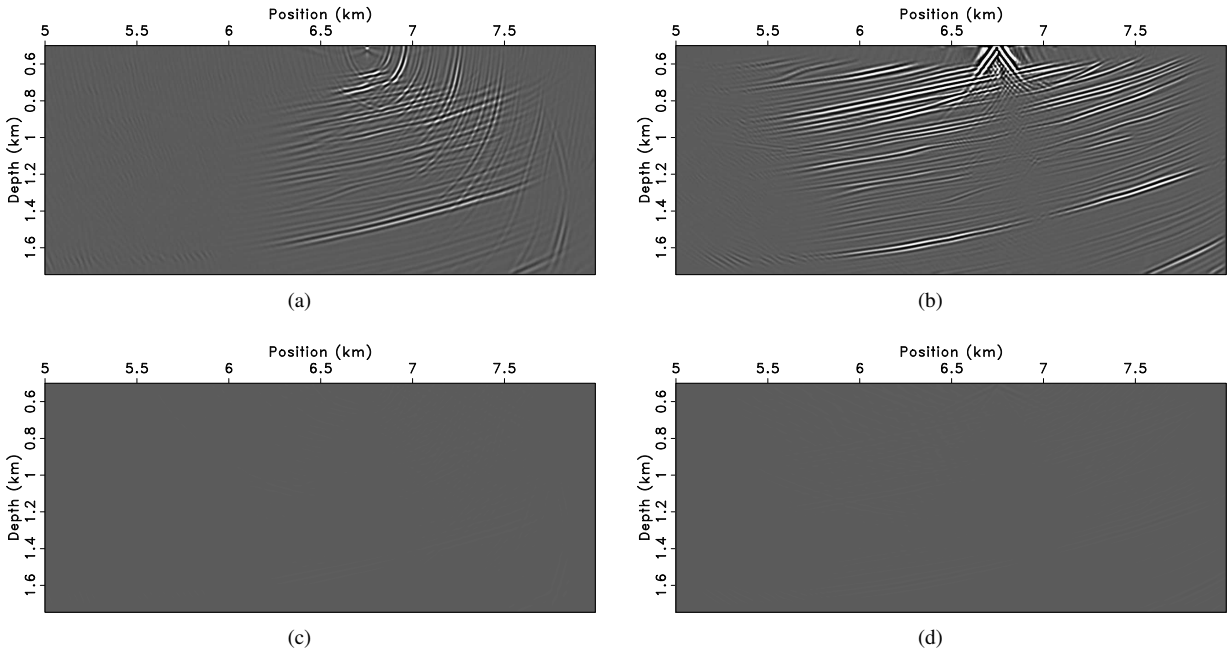


Figure 6. Images produced with the scalar and vector potentials imaging condition, equation 7. (a), (b), (c) and (d) correspond to the cross-correlation of the P and S components of the source wavefield with the P and S components of the receiver wavefield, respectively.The image corresponds to one shot at position $x = 6.75$ km and $z = 0.5$ km. Receivers are located at all locations at $z = 0.5$ km.

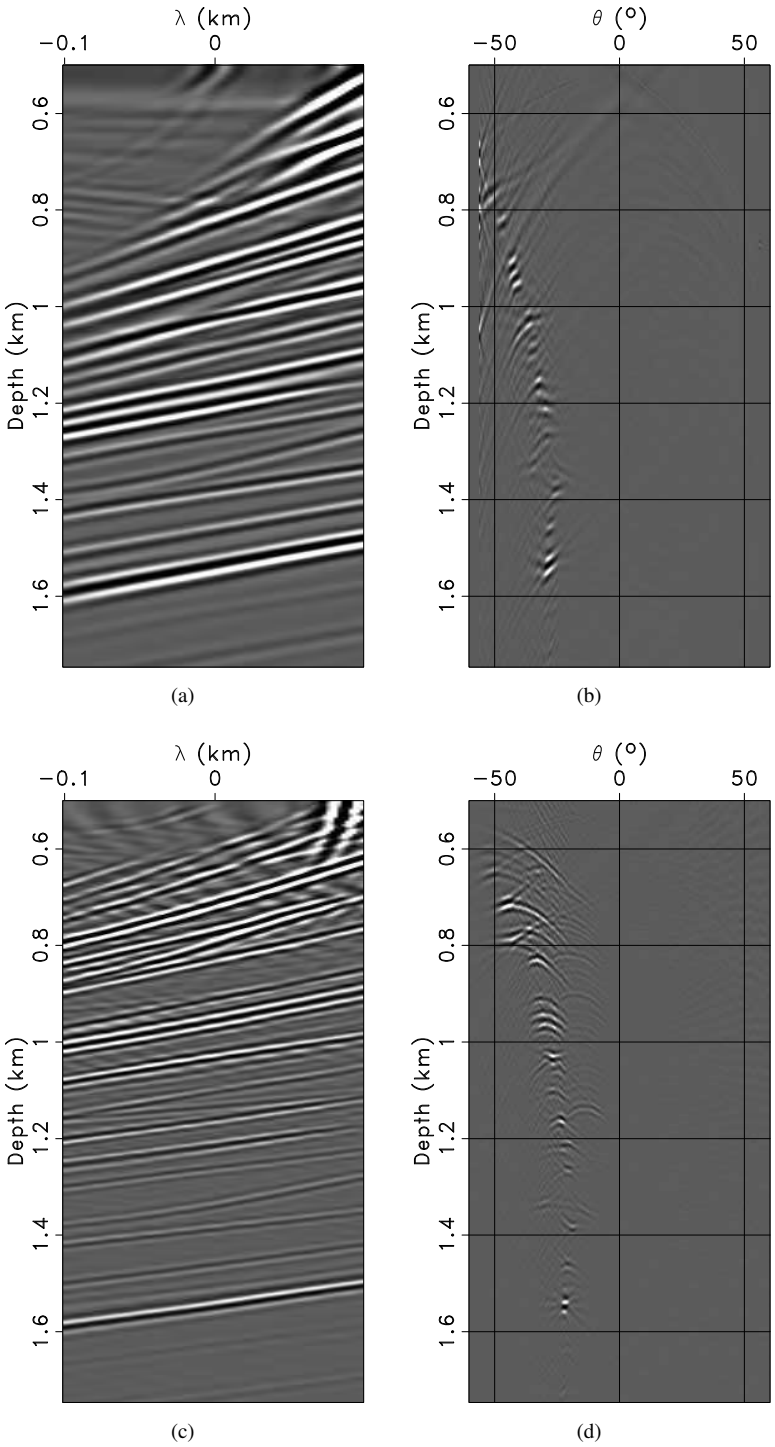


Figure 7. Horizontal cross-correlation lags for (a) PP and (c) PS reflections for model in Figures 3(a) and 3(b). The source is at $x = 6.75$ km, and the CIG is located at $x = 6.5$ km. Panels (b) and (d) depict PP and PS angle gathers decomposed from the horizontal lag gathers in panels (a) and (c), respectively. As expected, PS angles are smaller than PP angles for a particular reflector due to smaller reflection angles.

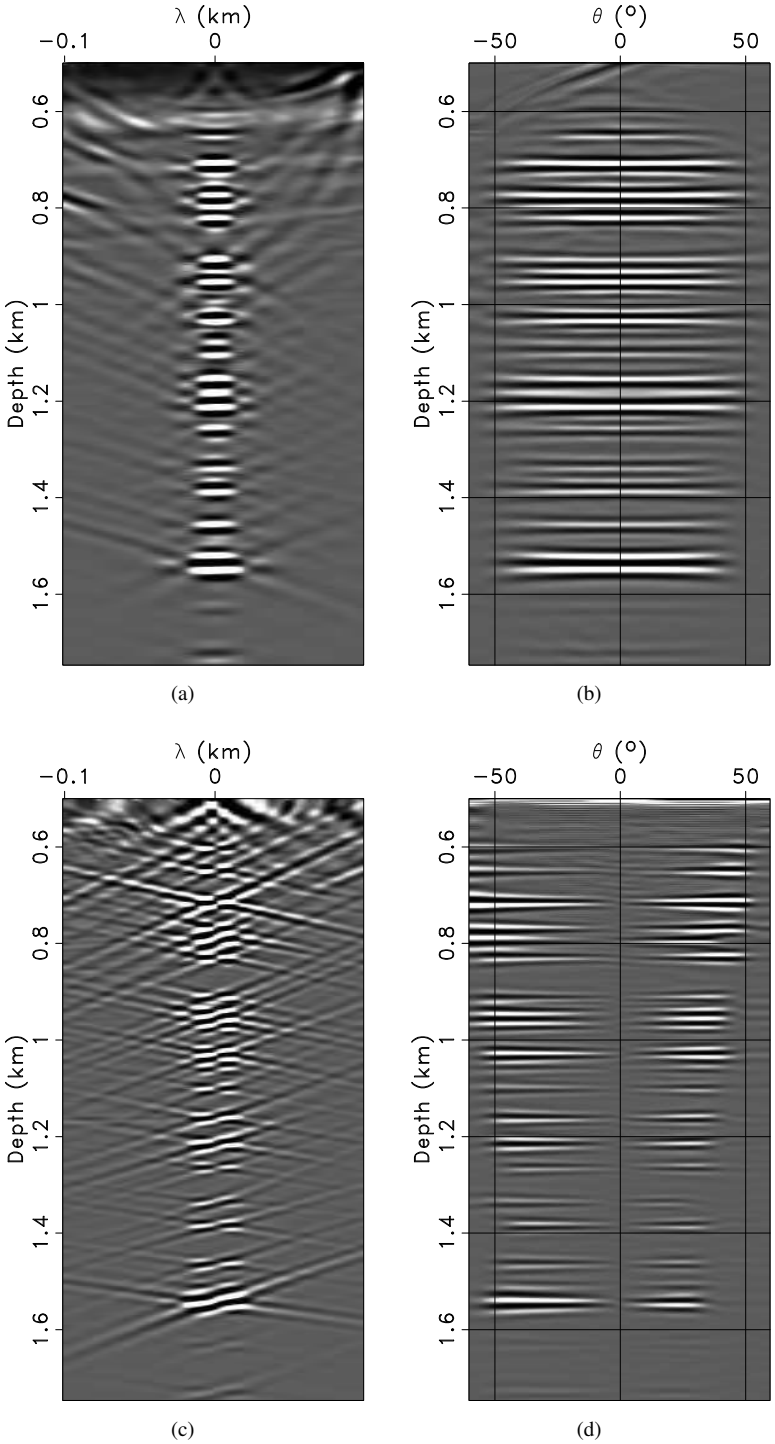


Figure 8. Horizontal cross-correlation lags for PP (a) and PS (c) reflections for model in Figures 3(a) and 3(b). These CIGs correspond to 81 sources from $x = 5.5$ to 7.5 km at $z = 0.5$ km. The CIG is located at $x = 6.5$ km. Panels (b) and (d) depict PP and PS angle gathers decomposed from the horizontal lag gathers in panels (a) and (c), respectively. Since the velocity used for imaging is correct, the PP and PS gathers are flat. The PP angle gathers do not change polarity at normal incidence, but the PS angle gathers change polarity at normal incidence.

REFERENCES

Aki, K., and Richards, P., 2002, Quantitative seismology (second edition): , University Science Books.

Alford, R. M., Kelly, K. R., and Boore, D. M., 1990, Accuracy of finite-difference modeling of the acoustic wave equation *in* Marfurt, K. J., Ed., Numerical modeling of seismic wave propagation:: Soc. of Expl. Geophys., 310–318.

Baysal, E., Kosloff, D. D., and Sherwood, J. W. C., 1983, Reverse time migration: Geophysics, **48**, no. 11, 1514–1524.

Boechat, J. B., Bulcão, A., Filho, D. M. S., Cunha, P. M., Mansur, W. J., and Moreira, T., 2007, A 3D reverse-time migration scheme for offshore seismic data: SEG Technical Program Expanded Abstracts, **26**, no. 1, 2427–2431.

Bolt, B. A., and Smith, W. D., 1976, Finite-element computation of seismic anomalies for bodies of arbitrary shape (short note): Geophysics, **41**, no. 01, 145–151.

Chang, W.-F., and McMechan, G. A., 1986, Reverse-time migration of offset vertical seismic profiling data using the excitation-time imaging condition: Geophysics, **51**, no. 1, 67–84.

Chang, W.-F., and McMechan, G. A., 1994, 3-D elastic prestack, reverse-time depth migration: Geophysics, **59**, no. 4, 597–609.

Claerbout, J. F., 1971, Toward a unified theory of reflector mapping: Geophysics, **36**, no. 03, 467–481.

Claerbout, J. F., 1985, Imaging the Earth's interior: , Blackwell Scientific Publications.

Cunha Filho, C., 1992, Elastic modeling and migration in earth models: , PhD thesis, Stanford University.

Dablain, M. A., 1986, The application of high-order differencing to the scalar wave equation: Geophysics, **51**, no. 01, 54–66.

Dai, N., and Cheadle, S., 1996, Pseudo-spectral migration in the F-X domain: Pseudo-spectral migration in the F-X domain:, Soc. of Expl. Geophys., 66th Ann. Internat. Mtg, 427–430.

Dellinger, J., and Etgen, J., 1990, Wave-field separation in two-dimensional anisotropic media (short note): Geophysics, **55**, no. 07, 914–919.

Etgen, J. T., 1988, Prestacked migration of P and Sv-waves: Prestacked migration of P and Sv-waves:, Soc. of Expl. Geophys., 58th Ann. Internat. Mtg, Session:S12.4.

Fomel, S., and Backus, M., 2003, Multicomponent seismic data registration by least squares: Multicomponent seismic data registration by least squares:, Soc. of Expl. Geophys., 73rd Ann. Internat. Mtg., 781–784.

Gray, S. H., Etgen, J., Dellinger, J., and Whitmore, D., 2001, Seismic migration problems and solutions: Geophysics, **66**, no. 5, 1622–1640.

Hokstad, K., Mittet, R., and Landro, M., 1998, Elastic reverse time migration of marine walkaway vertical seismic profiling data: Geophysics, **63**, no. 05, 1685–1695.

Hokstad, K., 2000, Multicomponent Kirchhoff migration: Geophysics, **65**, no. 3, 861–873.

Jones, I. F., Goodwin, M. C., Berranger, I. D., Zhou, H., and Farmer, P. A., 2007, Application of anisotropic 3D reverse time migration to complex North Sea imaging: SEG Technical Program Expanded Abstracts, **26**, no. 1, 2140–2144.

Kuo, J. T., and Dai, T. F., 1984, Kirchhoff elastic wave migration for the case of noncoincident source and receiver: Geophysics, **49**, no. 08, 1223–1238.

Levin, S. A., 1984, Principle of reverse-time migration: Geophysics, **49**, no. 5, 581–583.

Martin, G., Marfurt, K., and Larsen, S., 2002, Marmousi-2: An updated model for the investigation of AVO in structurally complex areas: Marmousi-2: An updated model for the investigation of AVO in structurally complex areas:, Soc. of Expl. Geophys., 72nd Ann. Internat. Mtg, 1979–1982.

Mora, P. R., 1987, Nonlinear two-dimensional elastic inversion of multioffset seismic data: Geophysics, **52**, no. 09, 1211–1228.

Mora, P., 1988, Elastic wave-field inversion of reflection and transmission data: Geophysics, **53**, no. 06, 750–759.

Nickel, M., and Sonneland, L., 2004, Automated PS to PP event registration and estimation of a high-resolution Vp-Vs ratio volume: Automated PS to PP event registration and estimation of a high-resolution Vp-Vs ratio volume:, Soc. of Expl. Geophys., 74th Ann. Internat. Mtg., 869–872.

Pestana, R. C., da Mota, F. M. R., Ulrych, T. J., Freire, S., and da Silva, F. B., 1989, Deterministic and stochastic separation of P and Sv-waves: A comparison: Deterministic and stochastic separation of P and Sv-waves: A comparison:, Soc. of Expl. Geophys., 59th Ann. Internat. Mtg, 1308.

Sava, P., and Fomel, S., 2003, Angle-domain common image gathers by wavefield continuation methods: Geophysics, **68**, no. 3, 1065–1074.

Sava, P., and Fomel, S., 2006a, Time-shift imaging condition for converted waves: SEG Technical Program Expanded Abstracts, **25**, no. 1, 2460–2464.

——— 2006b, Time-shift imaging condition in seismic migration: Geophysics, **71**, no. 6, S209–S217.

Seriani, G., and Priolo, E., 1991, High-order spectral element method for acoustic wave modeling: High-order spectral element method for acoustic wave modeling:, Soc. of Expl. Geophys., 61st Ann. Internat. Mtg, 1561–1564.

Seriani, G., Priolo, E., Carcione, J., and Padovani, E., 1992, High-order spectral element method for elastic wave modeling: High-order spectral element method for elastic wave modeling:, Soc. of Expl. Geophys., 62nd Ann. Internat. Mtg, 1285–1288.

Simmons, J., and Backus, M., 2003, An introduction—Multicomponent: The Leading Edge, **22**, no. 12, 1227–1262.

Sun, R., McMechan, G. A., Lee, C.-S., Chow, J., and Chen, C.-H., 2006, Prestack scalar reverse-time depth migration of 3D elastic seismic data: Geophysics, **71**, no. 5, S199–S207.

Virieux, J., 1984, SH-wave propagation in heterogeneous media - Velocity-stress finite-difference method: Geophysics, **49**, no. 11, 1933–1942.

Virieux, J., 1986, P-Sv wave propagation in heterogeneous media - Velocity-stress finite-difference method: Geophysics, **51**, no. 04, 889–901.

Whitmore, N. D., 1983, Iterative depth migration by back-

ward time propagation: Iterative depth migration by backward time propagation:, Soc. of Expl. Geophys., 53rd Ann. Internat. Mtg, Session:S10.1.

Zhe, J., and Greenhalgh, S. A., 1997, Prestack multicomponent migration: Geophysics, **62**, no. 02, 598–613.